FOREX Publication
Open Access | Rapid and quality publishing

International Journal of Electrical and Electronics Research (IJEER)
Research Article | Volume 13, Issue 4 | Pages 756-771 | e-ISSN: 2347-470X

Beluga Whale Optimization (BWO) Algorithm for Maximum Power Point Tracking from PV System for an Open-End Winding Induction Motor Drive with MPC-SVM Modulation

Balakrishna Kothapalli[1]*, and Dr. G T Sundar Rajan[2]
[1]*Research Scholar, EEE Department, Sathyabama Institute of Science and Technology, Chennai, India; kotapallibalakrishna@gmail.com*
[2]*Professor, EEE Department, Sathyabama Institute of Science and Technology, Chennai, India; Email: Sundarrajan.eee@sathyabama.ac.in*

***Correspondence:** *Balakrishna Kothapalli, Email: kotapallibalakrishna@gmail.com*

ABSTRACT- This paper presents a novel control framework integrating the Beluga Whale Optimization (BWO) algorithm for Maximum Power Point Tracking (MPPT) in photovoltaic (PV) systems driving an Open-End Winding Induction Motor (OEWIM) using a Model Predictive Control–Space Vector Modulation (MPC–SVM) strategy. The BWO algorithm, inspired by the intelligent hunting behaviour of beluga whales, is employed to dynamically extract the global maximum power point under varying irradiance and temperature conditions, enhancing PV efficiency. The extracted power feeds a dual-inverter OEWIM drive, which offers greater voltage flexibility and fault tolerance compared to conventional topologies. To ensure optimal current quality and torque performance, the MPC–SVM scheme predicts future motor states and applies an optimized voltage vector synthesized via space vector modulation. The system also incorporates discrete-time current modelling, delay compensation, virtual voltage vector generation, and dead-time compensation to address practical implementation challenges. Simulation results validate the superiority of the proposed BWO-MPPT and MPC–SVM-driven OEWIM architecture in achieving rapid MPPT convergence, reduced current ripple, improved torque stability, and high system efficiency under dynamic operating conditions. This integrated approach is highly suitable for renewable energy-based electric drive applications in smart grid and industrial automation environments.

Keywords: Beluga Whale Optimization (BWO), Maximum Power Point Tracking (MPPT), Open-End Winding Induction Motor (OEWIM), Model Predictive Control (MPC), Space Vector Modulation (SVM), Photovoltaic (PV) System.

ARTICLE INFORMATION
Author(s): Balakrishna Kothapalli, Dr. G T Sundar Rajan;
Received: 18/06/2025; **Accepted:** 28/10/2025; **Published:** 15/12/2025;
E- ISSN: 2347-470X;
Paper Id: IJEER 1806-11;
Citation: 10.37391/ijeer.130416
Webpage-link:
https://ijeer.forexjournal.co.in/archive/volume-13/ijeer-130416.html

Publisher's Note: FOREX Publication stays neutral with regard to jurisdictional claims in Published maps and institutional affiliations.

1. INTRODUCTION

The integration of photovoltaic (PV) systems with motor drives is critical for energy efficiency, but the nonlinear nature of PV sources necessitates robust maximum power point tracking (MPPT) to maximize energy harvest [1, 2]. For the motor drive, the open-end winding induction motor (OEWIM) offers a superior voltage envelope and fault tolerance but requires advanced modulation techniques [3, 4]. Model Predictive Control (MPC) coupled with Space Vector Modulation (SVM) has emerged as a powerful solution for OEWIMs, enabling high-fidelity control with minimized current ripple [5]. A significant challenge, however, is the computational burden of traditional MPC, which can limit real-time implementation [6]. This creates a critical gap for a computationally efficient control scheme that does not compromise the dynamic performance of the PV-fed OEWIM system, which this work aims to address.

For PV energy extraction under partial shading, metaheuristic algorithms are essential to avoid local optima [7]. The Beluga Whale Optimization (BWO) algorithm is particularly noted for its effective balance between global exploration and local exploitation, leading to fast convergence on the global maximum power point [8]. Recent research has focused on enhancing such algorithms through adaptation and hybridization. For instance, modified versions of established optimizers have been developed to dynamically adjust parameters based on real-time PV curve conditions, improving both speed and accuracy [9, 10]. Furthermore, a prominent trend involves embedding these algorithms within artificial neural networks for forecasting or hybridizing them with conventional methods [11, 12]. These hybrid bio-inspired strategies are now considered state-of-the-art for complex shading scenarios, as they achieve rapid transients and minimal steady-state oscillation [13].

Recent advancements have significantly enhanced the Beluga Whale Optimization (BWO) algorithm, reinforcing its potential

FOREX Publication
Open Access | Rapid and quality publishing
International Journal of Electrical and Electronics Research (IJEER)
Research Article | Volume 13, Issue 4 | Pages 756-771 | e-ISSN: 2347-470X

for engineering applications. Its capabilities have been extended through hybridization with other metaheuristics, resulting in superior performance against multiple benchmarks [14]. Further modifications, incorporating adaptive learning and Lévy flight strategies, have demonstrated statistically superior results on standardized test suites and engineering problems [15]. Moreover, embedding an enhanced BWO within an extreme learning machine for PV forecasting has proven effective for managing weather variability, confirming its robustness and adaptability [16]. These developments collectively affirm BWO as a versatile and powerful optimizer, well-suited for the complex MPPT task in this study.

Concurrently, significant progress has been made in predictive control for motor drives. For Open-End Winding Induction Motors (OEWIMs), Model Predictive Control (MPC) is now an established high-performance strategy. Research has yielded model-free predictive controllers that substantially reduce computational load [17] and successfully extended these methods to medium-voltage applications with integrated harmonic suppression [18]. Studies have confirmed that predictive torque control for dual-inverter systems can achieve dynamic performance rivaling multilevel converters [19]. However, these approaches still face real-time computational constraints, highlighting a need for more efficient formulations. A parallel research focus addresses the challenge of dead-time effects, which remain a critical bottleneck for precision torque control, especially with continuous modulation schemes like SVM. Recent solutions include adaptive notch filters for harmonic cancellation [20] and refined dead-time models leveraging fast-switching semiconductors [21]. Earlier compensation techniques using Kalman filters also provide a foundation for seamless integration with SVM [22].

A systematic review confirms that whale-family optimizers like BWO offer superior convergence and balance but require application-specific adaptation [23]. Critically, a clear research gap persists: no existing work integrates an intelligent, adaptive BWO-based MPPT with a computationally efficient, predictive control scheme for an OEWIM drive. Furthermore, existing dead-time compensation methods are not co-designed with such a unified virtual-vector MPC framework. This study aims to bridge this gap by proposing a cohesive system that synergistically combines these advanced elements to optimize overall performance.

This paper proposes an integrated control architecture that unites BWO-based MPPT and an MPC–SVM scheme for driving an OEWIM from a PV source. The major contributions are fourfold: *(i)* a discrete-time BWO algorithm tailored for MPPT that delivers rapid and robust convergence under stochastic irradiance profiles; *(ii)* a delay-compensated MPC predictor and cost function customized for the dual-inverter, open-end-winding topology; *(iii)* a virtual-vector, dead-beat SVM routine that slashes computational complexity while preserving optimality; and *(iv)* a practical dead-time compensation layer that mitigates nonlinear voltage errors. Comprehensive simulations demonstrate that the proposed framework yields superior tracking efficiency, reduced torque ripple and improved dynamic performance compared with state-of-the-art MPPT and control strategies. *Figure 1* illustrates the detailed system incorporating the proposed BWO-based MPPT algorithm for the PV system alongside a MPC-SVM modulation for OEWIM drives. The findings highlight the feasibility and advantages of deploying intelligent optimization and predictive modulation in renewable-powered industrial drive systems, thereby advancing the vision of sustainable and high-performance electrification.

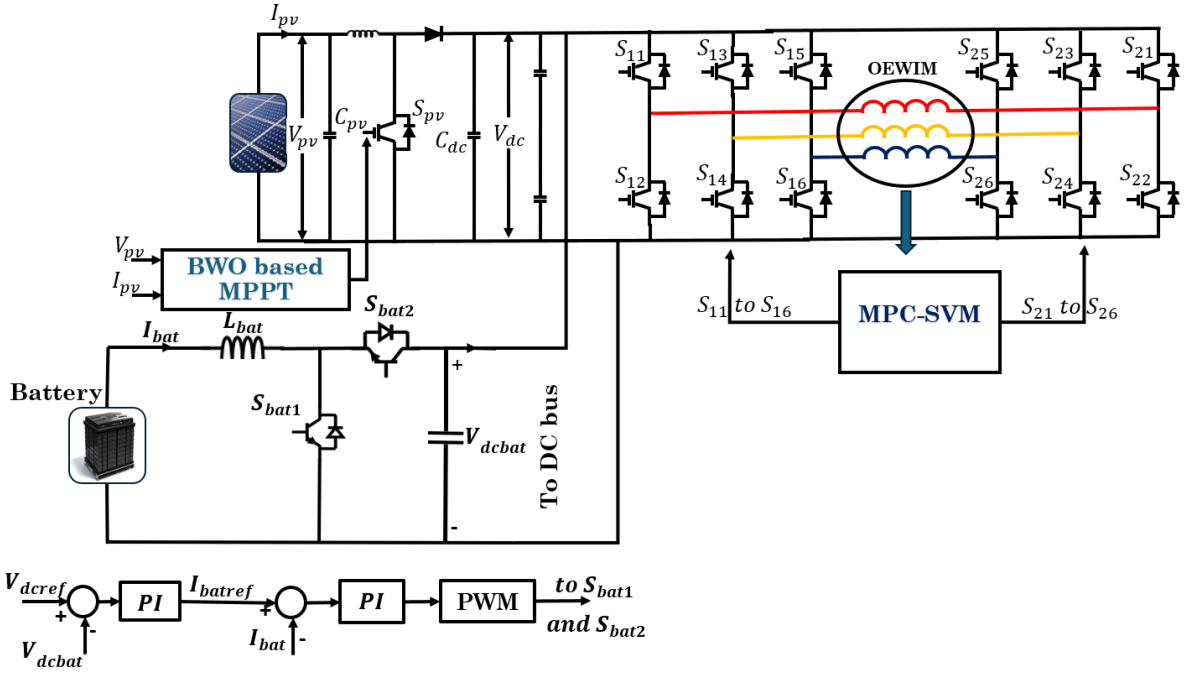

Figure 1. PV fed OEWIM with proposed MPPT and MPC-SVM

FOREX Publication
Open Access | Rapid and quality publishing
International Journal of Electrical and Electronics Research (IJEER)
Research Article | Volume 13, Issue 4 | Pages 756-771 | e-ISSN: 2347-470X

2. SYSTEM MODELLING

2.1. Mathematical model of Open-end winding IM

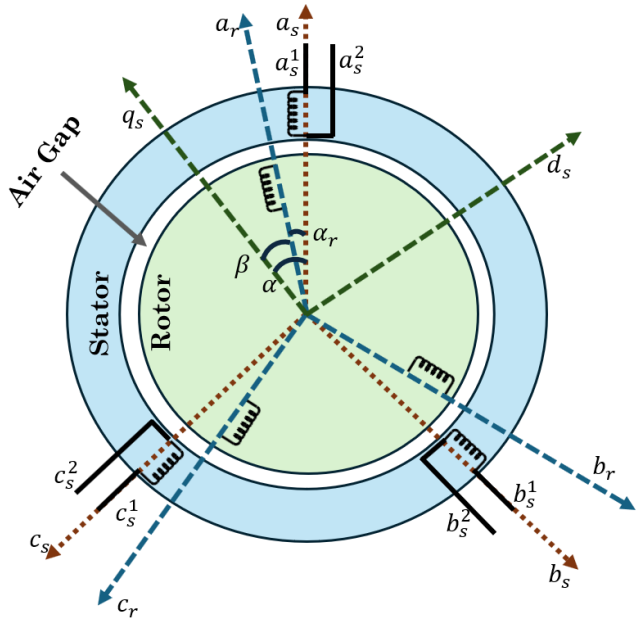

Figure 2. Vector representation of OEWIM Model

An Open-End Winding Induction Motor (OEWIM) is physically realized by ensuring that the stator windings remain unshorted, resulting in six stator terminals: a_s^1', 'a_s^2', 'b_s^1', 'b_s^2', 'c_s^1', *and* 'c_s^1 'c_s^2', *and* 'c_s^3', as depicted in *figure 2*. Meanwhile, the rotor windings remain shorted and unchanged, represented by the'a_r', 'b_r', *and* '$c_r$axes. The rotor is positioned at an angular offset, denoted as 'α_r', relative to the 'a_s^1' reference axis, as illustrated in *figure 2*.

$$\begin{bmatrix} v_{as} \\ v_{bs} \\ v_{cs} \end{bmatrix} = \begin{bmatrix} r_s & 0 & 0 \\ 0 & r_s & 0 \\ 0 & 0 & r_s \end{bmatrix} \begin{bmatrix} i_{as} \\ i_{bs} \\ i_{cs} \end{bmatrix} + p \begin{bmatrix} \lambda_{as} \\ \lambda_{bs} \\ \lambda_{cs} \end{bmatrix} \quad (1)$$

Here, λ_{as}, λ_{bs} and λ_{cs} represent the flux linkages of the respective stator phase windings, while r_s denotes the per-phase stator winding resistance. The corresponding stator phase currents are given by i_{as}, i_{bs} and i_{cs}.

In an OEWIM, the three-phase stator voltages can be transformed into the dq reference frame using a power-invariant transformation. This conversion shifts the voltages from a stationary to a rotating reference frame, simplifying the analysis and control of the motor. The relationship between the three-phase stator voltages $v_{as}, v_{bs}, and\ v_{cs}$ and the dq components v_{ds} and v_{qs} is expressed through the following power-invariant transformation:

$$\begin{bmatrix} v_{qs} \\ v_{ds} \\ v_0 \end{bmatrix} = \frac{2}{3} \begin{bmatrix} \cos(u) & \cos\left(u - \frac{2\pi}{3}\right) & \cos\left(u + \frac{2\pi}{3}\right) \\ \sin(u) & \sin\left(u - \frac{2\pi}{3}\right) & \sin\left(u + \frac{2\pi}{3}\right) \\ \frac{1}{2} & \frac{1}{2} & \frac{1}{2} \end{bmatrix} \begin{bmatrix} v_{as} \\ v_{bs} \\ v_{cs} \end{bmatrix} \quad (2)$$

In this transformation, v_{qs} denotes the quadrature-axis voltage component, while v_{ds} represents the direct-axis voltage component. The term $v_0$corresponds to the zero-sequence component, which is generally zero in a balanced three-phase system. The angle $u = \alpha$ represents the electrical angular position of the reference frame. Here, α defines the angle between the stator reference axis $a_s$and the q-axis, while β denotes the angle between the rotor reference axis a_r and the q-axis. Similarly, β represents the angle between the rotor reference axis $a_r$and the q-axis. The relative displacement between the stator and rotor reference axes is given by $\alpha_r = \alpha - \beta$, where α_r defines the angular difference between the stator and rotor frames. This d–q transformation simplifies motor analysis by enabling decoupled control of flux and torque components, which is essential for achieving efficient and precise motor operation.

$$v_{qs} = i_{qs} r_s + \omega \lambda_{ds} + \frac{d\lambda_{qs}}{dt} \quad (3)$$

$$v'_{qr} = i'_{qr} r'_r + (\omega - \omega_r)\lambda'_{dr} + \frac{d\lambda'_{qr}}{dt} \quad (4)$$

$$v_{ds} = i_{ds} r_s - \omega \lambda_{qs} + \frac{d\lambda_{ds}}{dt} \quad (5)$$

$$v'_{dr} = i'_{dr} r'_r - (\omega - \omega_r)\lambda'_{qr} + \frac{d\lambda'_{dr}}{dt} \quad (6)$$

The rotor's angular velocity, denoted as ω_r , represents the instantaneous speed of the motor shaft in radians per second, while ω denotes the synchronous speed of the machine. The synchronous speed of the machine is denoted by ω. In the case of a squirrel-cage induction motor, which is commonly used in simulations, the rotor-side voltages in the d–q frame, specifically $v_{dr}\ and\ v_{qr}$, are considered zero. This is because the rotor terminals are shorted, preventing any external voltage supply to the rotor windings.

The flux linkage equations for the OEWIM are stated as

$$\begin{bmatrix} \lambda_{qs} \\ \lambda_{ds} \\ \lambda'_{qr} \\ \lambda'_{dr} \end{bmatrix} = \begin{bmatrix} L_m + L_{ls} & 0 & L_m & 0 \\ 0 & L_m + L_{ls} & 0 & L_m \\ L_m & 0 & L_m + L'_{lr} & 0 \\ 0 & L_m & 0 & L_m + L'_{lr} \end{bmatrix} \begin{bmatrix} i_{qs} \\ i_{ds} \\ i'_{qr} \\ i'_{dr} \end{bmatrix} \quad (7)$$

Here, $L_m$denotes the magnetizing inductance, L_{ls} represents the stator winding leakage inductance, and L'_{lr} corresponds to the rotor winding leakage inductance referred to the stator.

These inductances play a crucial role in defining the flux linkage between the stator and rotor windings, directly impacting the motor's overall performance. The interaction between the stator and rotor flux linkages is governed by these inductances, influencing key operational characteristics such as torque production and efficiency. The electromagnetic torque T_m developed in the OEWIM is stated as;

$$T_e = \frac{3}{2}\frac{p}{2}\frac{L_m}{L_s}\left(\lambda_{qs} i'_{dr} - \lambda_{ds} i'_{qr}\right) \quad (8)$$

p is the number of poles of the machine. The mechanical equation governing the OEWIM-pump drive, which models the dynamics of the motor's rotational movement, is stated as:

FOREX Publication
Open Access | Rapid and quality publishing
International Journal of Electrical and Electronics Research (IJEER)
Research Article | Volume 13, Issue 4 | Pages 756-771 | e-ISSN: 2347-470X

$$J\frac{d\omega_r}{dt} + B\omega_r + T_L = T_e \quad (9)$$

J represents the moment of inertia of the OEWIM (measured in kg·m²), indicating the motor's resistance to changes in rotational motion. The parameter B denotes the centrifugal load torque coefficient, accounting for friction and other opposing forces that resist the motor shaft's movement. The torque T_L represents the external load torque applied to the system, while the right-hand side of the equation corresponds to the developed electromagnetic torque T_e, which drives the motor's motion. These equations collectively define the dynamic behaviour of the OEWIM, incorporating both its electrical and mechanical characteristics.

2.2. Mathematical Model of PV Array Power Loss

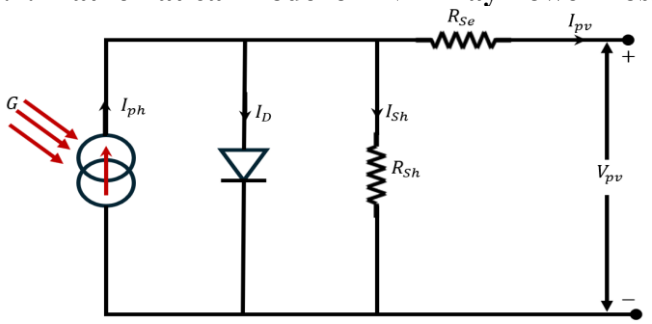

Figure 3. Equivalent circuit of PV Panel

The single-diode model of a PV panel is illustrated in *figure 3*. The photocurrent's relationship with solar irradiance is expressed as follows:

$$I_{ph} = I_{sc} \times \frac{G}{G_{ref}} \quad (10)$$

Here, I_{sc} represents the short-circuit current under standard test conditions, GGG is the instantaneous solar irradiance, and G_{ref} denotes the reference irradiance (typically 1000 W/m²). The equivalent circuit of a PV cell consists of a current source in parallel with a diode, along with a series resistance R_{Se}, which accounts for internal losses caused by the semiconductor material's resistance. The diode represents the *p-n* junction of the solar cell and models the recombination of charge carriers. The output current I_{pv} from the solar cell is determined by the Shockley diode equation, which is modified to incorporate the photocurrent.

$$I_{pv} = I_{ph} - I_D - I_{Sh} \quad (11)$$

$$I_D = I_0\left(\exp\left(\frac{V_{pv}+R_{Se}I_{pv}}{AN_sV_t}\right) - 1\right) \quad (12)$$

$$I_{Sh} = \frac{(V_{pv}+R_{Se}I_{pv})}{R_{Sh}} \quad (13)$$

$$V_t = \frac{k\times V_{pv}}{q} \quad (14)$$

Here, V_{pv} represents the PV cell voltage, while I_{pv} denotes the generated current. R_{Se} and R_{Sh} correspond to the series and parallel resistances, respectively. $N_s$indicates the number of cells connected in series within a module. Additionally, V_t is the thermal voltage, q represents the electron charge, and I_0 denotes the diode saturation current.

The power output of a PV system is strongly influenced by environmental factors, particularly solar irradiance and temperature. Due to the nonlinear characteristics of a PV panel, its output varies with changing conditions. At any given time, the maximum power that can be extracted occurs at a specific operating point, referred to as the Maximum Power Point (MPP). The location of the Maximum Power Point (MPP) continuously shifts with variations in sunlight intensity and temperature. Without an effective tracking mechanism, the PV system would operate at a suboptimal point, leading to reduced energy conversion efficiency. Maximum Power Point Tracking (MPPT) algorithms are employed to dynamically adjust the operating point of the PV system, ensuring it consistently operates at the MPP despite fluctuations in solar irradiance or temperature.

2.3. Battery with Bidirectional Converter

In the proposed HBWO-based MPPT algorithm for PV systems and the improved DTC strategy for OEWIM drives, a battery with a bidirectional converter is integrated into the system. The primary purpose of this battery is to ensure a continuous and stable power supply to the motor, even under fluctuating solar power conditions. Since PV systems inherently exhibit intermittent power generation due to variations in solar irradiance and temperature, the battery plays a crucial role in maintaining the DC link voltage stability and ensuring uninterrupted motor operation. The bidirectional converter facilitates both charging and discharging of the battery, effectively managing energy flow between the PV system, battery, and the motor drive system.

The bidirectional converter enables controlled power exchange between the battery and the DC link. During excess PV power generation, the surplus energy is stored in the battery by operating the converter in buck mode, reducing the voltage to match the battery's charging requirements. Conversely, when the PV power is insufficient to meet the motor's demand, the stored energy in the battery is supplied to the DC link through the converter operating in boost mode, ensuring continuous power availability. This dynamic energy management enhances system reliability and efficiency, preventing voltage fluctuations that could affect motor performance. *Figure 4* presents the battery energy storage system with bidirectional converter and its control strategy.

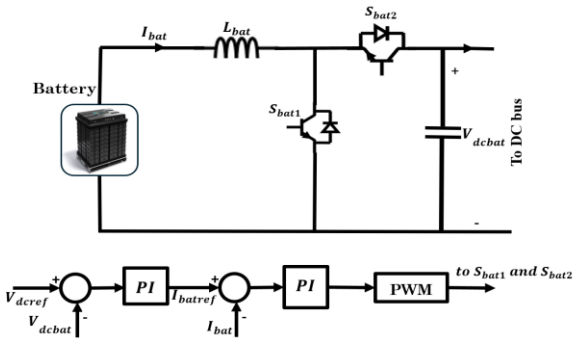

Figure 4. Battery energy storage system with bidirectional converter and its control strategy

FOREX Publication
Open Access | Rapid and quality publishing
International Journal of Electrical and Electronics Research (IJEER)
Research Article | Volume 13, Issue 4 | Pages 756-771 | e-ISSN: 2347-470X

To regulate the DC link voltage and ensure efficient power exchange, a dual-loop control strategy is implemented in the bidirectional converter. This control strategy consists of an outer voltage control loop and an inner current control loop, working together to maintain the desired power flow and system stability as presented in *equation (15)* and *(16);*

$$I_{batref} = K_{pv}\left(V_{dcref}(t) - V_{dcbat}(t)\right) + K_{iv}\int\left(V_{dcref}(t) - V_{dcbat}(t)\right)dt \quad (15)$$

K_{pv} and K_{iv} are PI controller gains, V_{dcref} DC link reference voltage, V_{dcbat} actual DC link voltage,

$$d_{bat} = K_{pi}\left(I_{batref}(t) - I_{bat}(t)\right) + K_{ii}\int\left(I_{batref}(t) - I_{bat}(t)\right)dt \quad (16)$$

K_{pi} and K_{ii} are PI controller gains, I_{batref} battery reference current, I_{bat} actual battery current, The outer voltage control loop is responsible for regulating the DC link voltage. A reference DC link voltage is set, and the actual DC link voltage is continuously monitored. The error between the reference and actual voltage is processed by a PI controller, which generates a reference current for the inner current control loop. This ensures that the DC link voltage remains stable regardless of fluctuations in PV power or load demand, thereby maintaining steady operation of the OEWIM drive.

The inner loop regulates the battery current to ensure smooth power transfer. The reference current obtained from the outer loop is compared with the actual current flowing through the bidirectional converter. A PI controller processes this error and generates the required duty cycle for PWM control. The PWM signals are used to switch the bidirectional converter, adjusting its operation mode (buck or boost) based on power demand.

During motor acceleration or increased load conditions, the inner loop allows the battery to supply power to the DC link by boosting the voltage. Conversely, when the PV system generates excess power, the converter operates in buck mode, transferring surplus energy to charge the battery efficiently. The coordinated control of these loops ensures that power flow is dynamically adjusted, preventing voltage instability and improving overall system performance.

3. BELUGA WHALE OPTIMIZATION (BWO)

3.1. Mathematical Model of Beluga Whale Optimization

The BWO algorithm is inspired by the natural behaviours of beluga whales, such as swimming, preying, and the phenomenon of whale fall. In a manner like other metaheuristic algorithms, BWO operates with two main phases: the exploration phase and the exploitation phase. The exploration phase ensures a global search capability within the design space by randomly selecting beluga whales, which allows the algorithm to explore a wide range of potential solutions. The exploitation phase focuses on a local search within the design space, optimizing the identified potential solutions. This two-phase structure is essential for the algorithm's efficiency, as it combines the ability to search broadly (exploration) with the ability to fine-tune solutions (exploitation).

The population-based nature of the BWO algorithm considers the group of beluga whales as a population of search agents. Each individual whale represents a candidate solution, and its position in the search space corresponds to a potential solution to the optimization problem at hand. The positions of the beluga whales are represented as a matrix, where each row corresponds to a beluga whale, and each column corresponds to a design variable. The matrix is formulated as;

$$X = \begin{bmatrix} x_{1,1} & x_{1,2} & \cdots & x_{1,d} \\ x_{2,1} & x_{2,2} & \cdots & x_{2,d} \\ \vdots & \vdots & \ddots & \vdots \\ x_{n,1} & x_{n,2} & \cdots & x_{n,d} \end{bmatrix} \quad (17)$$

In this matrix, n represents the population size of the beluga whales, and d denotes the dimension of the design variables. Each element in the matrix, $x_{i,j}$, indicates the position of the i-th beluga whale in the j-th dimension of the design space. The corresponding fitness values of these beluga whales (or candidate solutions) are stored in a vector, F_X, where each element represents the fitness of the corresponding solution:

$$F_x = \begin{bmatrix} f(x_{1,1}, x_{1,2}, \ldots, x_{1,d}) \\ f(x_{2,1}, x_{2,2} \ldots, x_{2,d}) \\ \vdots \\ f(x_{n,1}, x_{n,2}, \ldots, x_{n,d}) \end{bmatrix} \quad (18)$$

The fitness values are evaluated based on the specific optimization problem and guide the algorithm in determining which positions are more optimal.

A key feature of the BWO algorithm is its ability to switch between the exploration and exploitation phases, which is controlled by a balance factor B_f. This balance factor governs the probability of the algorithm being in either phase. It is modelled as:

$$B_f = B_0\left(1 - \frac{T}{2T_{max}}\right) \quad (19)$$

Here, T represents the current iteration number, T_{max} is the maximum number of iterations, and B_0 is a random value between 0 and 1 that changes at each iteration. The balance factor B_f decreases as the algorithm progresses, starting from a value between 0 and 1 and gradually shifting towards 0.5. When B_f is greater than 0.5, the algorithm is in the exploration phase, which encourages broad searching across the solution space. When B_f becomes less than or equal to 0.5, the algorithm transitions into the exploitation phase, which focuses on refining the solutions locally. As the iterations progress, the fluctuation range of B_f shrinks from (0, 1) to (0, 0.5), signifying that the algorithm increasingly focuses on exploitation rather than exploration. This transition is a dynamic process that balances

FOREX Publication
Open Access | Rapid and quality publishing
International Journal of Electrical and Electronics Research (IJEER)
Research Article | Volume 13, Issue 4 | Pages 756-771 | e-ISSN: 2347-470X

the need to explore new regions of the search space with the necessity to exploit the promising regions already discovered. The gradual reduction in the exploration phase allows the algorithm to fine-tune its solutions, optimizing the search process over time.

3.1.1. Exploration Phase

The exploration phase in the BWO algorithm is modelled after the swimming behaviour of beluga whales, particularly the synchronized movements they exhibit during pair swimming. Beluga whales, especially those in human care, have been observed to engage in social-sexual behaviours under various postures, such as swimming closely together in pairs, often moving in a synchronized or mirrored manner. This behaviour serves as an inspiration for the BWO algorithm, where the positions of the search agents (beluga whales) are determined by this pair swimming dynamic. This synchronized or mirrored movement allows the algorithm to explore the solution space by adjusting the position of the whales in a way that mimics these natural behaviours. To mathematically model this behaviour, the algorithm updates the position of each search agent using the following equation;

$$X_{i,j}(T+1) = \begin{cases} X_{i,p_j}(T) + \left(X_{r,p_1}(T) - X_{r,p_j}(T)\right)(1+r_1)\sin(2\pi r_2), \text{when } j \text{ is even} \\ X_{i,p_j}(T) + \left(X_{r,p_1}(T) - X_{r,p_j}(T)\right)(1+r_1)\cos(2\pi r_2), \text{when } j \text{ is odd} \end{cases} \quad (20)$$

In these equations, $X_{i,j}(T+1)$ represents the updated position of the i-th beluga whale on the j-th dimension of the search space at the Tth iteration. The position update is based on the current position $X_{i,pj}(T)$ of the whale in the jth dimension, as well as the position of another randomly selected whale, denoted as $X_{r,p1}(T)$, where r is a randomly chosen whale from the population. The variables r_1 and r_2 are random numbers between 0 and 1, which are used to introduce randomness and variability in the movement. These random numbers ensure that the search is not deterministic, allowing the algorithm to explore a broader range of the solution space.

3.1.2. Exploitation Phase

The exploitation phase of BWO is inspired by the cooperative foraging behaviour of beluga whales. In this phase, the whales share information about their positions to aid in their search for prey. This allows them to converge on the best positions by using a strategy called Levy flight, which improves the efficiency of their movement and prey capture. The mathematical formulation of this phase involves several key components:

The position update for a given whale iii during the exploitation phase is given by:

$$X_i(T+1) = r_3 X_{best}(T) - r_4 X_i(T) + C_1 \times L_F \times \left(X_r(T) - X_i(T)\right) \quad (21)$$

Where $X_i(T)$ is the current position of the ith beluga whale, $X_r(T)$ is the position of a randomly selected whale., $X_{best}(T)$ is the best position found among all the whales, $X_i(T+1)$ represents the updated position of the ith whale after the iteration. r_3 and r_4 are random numbers generated between 0 and 1, C_1 is the random jump strength, defined as $C_1 = 2r_4\left(1 - \frac{T}{Tmax}\right)$, which decreases as the number of iterations increases, reflecting diminishing intensity of the Levy flight. L_F is the Levy flight function, which introduces random jumps into the search process to escape local optima. The Levy flight function (LF) is defined as:

$$L_F = 0.05 \times \frac{u \times \sigma}{|v|^{\frac{1}{\beta}}} \quad (22)$$

$$\sigma = \left(\frac{\Gamma(1+\beta) \times \sin\left(\frac{\pi\beta}{2}\right)}{\Gamma\left(\frac{(1+\beta)}{2}\right) \times \beta \times 2^{\frac{\beta-1}{2}}}\right)^{1/\beta} \quad (23)$$

Where Γ is the Gamma function, which generalizes the factorial function. Levy flight is a random walk process where the step sizes follow a power-law distribution, which allows the optimization algorithm to make large jumps with small probabilities. This enhances exploration during the exploitation phase. The introduction of Levy flight enables the beluga whales to efficiently search for prey by making random but strategically strong movements that help them avoid being stuck in local optima. The random jump strength C_1 varies throughout the iterations, becoming smaller as the process progresses, which reflects the balance between exploration (global search) and exploitation (local search).

3.1.3. Whale Fall

The phenomenon of whale fall refers to the process in which a beluga whale, having fallen to the deep seabed, becomes a source of nourishment for numerous marine creatures. To model the behaviour of whale fall in a computational environment, we introduce a method to simulate the changes in the population of beluga whales over time. The mathematical model used to update the position of each whale in the population is expressed as follows:

$$X_i(T+1) = r_5 X_i(T) - r_6 X_r(T) + r_7 X_{step}) \quad (24)$$

In this equation, r_5, r_6 and r_7 are random numbers between 0 and 1, and X_{step} represents the step size of the whale fall, which determines how much the position of each whale changes in the next iteration. The step size itself is calculated using the following formula;

$$X_{step} = (ub - lb)\exp\left(-\frac{C_2 T}{T_{max}}\right) \quad (25)$$

Here, C_2 is a step factor that is influenced by both the probability of whale fall and the size of the population. Specifically, $C_2 = 2W_f \times n$, where W_f is the probability of whale fall and n is the population size. ub and lb represent the upper and lower boundaries of the design variables, respectively. This step size function ensures that as the simulation progresses, the change in the positions of the whales gradually decreases, reflecting the diminishing likelihood of whale fall over time. The probability

FOREX Publication
Open Access | Rapid and quality publishing
International Journal of Electrical and Electronics Research (IJEER)
Research Article | Volume 13, Issue 4 | Pages 756-771 | e-ISSN: 2347-470X

of whale fall, W_f, is modelled as a linear function of the iteration number, decreasing from an initial value of 0.1 at the start of the simulation to 0.05 at the final iteration. This is given by the formula;

$$W_f = 0.1 - \frac{0.05T}{T_{max}} \quad (26)$$

The decreasing probability indicates that, as the whales approach the food source in the optimization process, the danger to their survival reduces.

3.1.4. Pseudocode for BWO Algorithm

```
% Step 1: Initialization
Initialize population size n (number of beluga whales)
Initialize maximum number of iterations Tmax
Initialize upper and lower bounds of the search space (ub, lb)
Initialize the positions of all beluga whales randomly within the search space
Calculate the fitness values of all whales based on the objective function

% Step 2: Main Loop for Optimization
for T = 1:Tmax
  % Step 2.1: Update on Exploration and Exploitation Phase
  for i = 1:n  % Iterate over each whale
    % Step 2.1.1: Calculate balance factor Bf for each whale
    Bf = rand();  % Randomly generate Bf (between 0 and 1)

    % Step 2.1.2: Determine which phase (exploration or exploitation) the whale enters
    if Bf > 0.5
      % Exploration Phase
      % Update whale position using exploration equation
      X_new(i,:) = X(i,:) + rand() * (X_best - X(i,:));  % Exploration formula

    else
      % Exploitation Phase
      % Update whale position using exploitation equation
      X_new(i,:) = X(i,:) + rand() * (X_best - X(i,:)) + rand() * (X_random - X(i,:));  % Exploitation formula
    end

    % Step 2.1.3: Calculate fitness of new position
    fitness_new = objective_function(X_new(i,:));

    % Step 2.1.4: Compare fitness and update if new position is better
    if fitness_new < fitness(i)
      X(i,:) = X_new(i,:);
      fitness(i) = fitness_new;
    end
  end

  % Step 2.2: Update on the Whale Fall Phase
  for i = 1:n

    % Step 2.2.1: Calculate probability of whale fall (Wf) for each iteration
    Wf = 0.1 - (0.05 * T / Tmax);  % Linearly decreasing probability

    % Step 2.2.2: Check if whale will fall (if randomly chosen)
    if rand() < Wf
      % Whale falls to the deep seabed
      % Update whale position using whale fall equation
      X_new(i,:) = r5 * X(i,:) - r6 * X_random + r7 * X_step;

      % Step 2.2.3: Calculate fitness of new position after whale fall
      fitness_new = objective_function(X_new(i,:));

      % Step 2.2.4: Update whale position if new fitness is better
      if fitness_new < fitness(i)
        X(i,:) = X_new(i,:);
        fitness(i) = fitness_new;
      end
    end
  end

  % Step 3: Find the best solution in the current iteration
  [best_fitness, best_index] = min(fitness);
  X_best = X(best_index, :);

  % Step 4: Check the termination condition (maximum iterations reached)
  if T == Tmax
    break;  % Exit the loop if the maximum number of iterations is reached
  end
end

% Output the final best solution found
disp('Best solution found:');
disp(X_best);
disp('Best fitness value:');
disp(best_fitness);
```

4. CONVENTIONAL MPC

Model Predictive Control (MPC) determines the optimal output value for the upcoming control period by evaluating a set of candidate input values based on the system's model equations. In order to accurately forecast the electrical torque and stator flux over each control interval, the stator voltage model must be converted into a discrete-time current model that aligns with the system's sampling interval. This transformation involves converting the continuous-time current equations, originally defined in terms of time t, into a discrete-time format that operates with respect to the sampling period T_s . To achieve this, the time derivatives present in the continuous model are approximated using finite difference expressions that estimate the rate of change between discrete sampling instances.

FOREX Publication
Open Access | Rapid and quality publishing
International Journal of Electrical and Electronics Research (IJEER)
Research Article | Volume 13, Issue 4 | Pages 756-771 | e-ISSN: 2347-470X

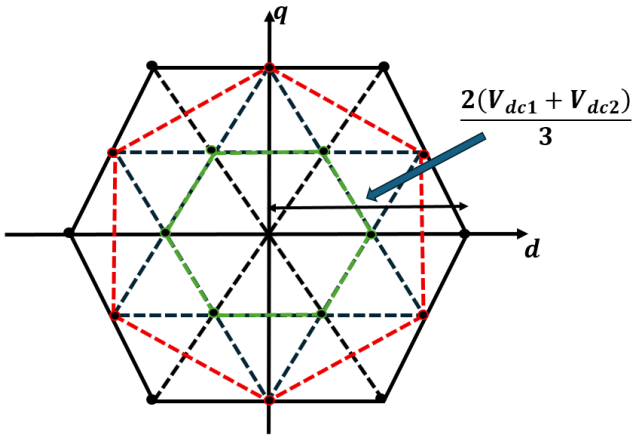

Figure 5. Voltage vector diagram of the dual inverter

For a short prediction horizon, it is customary to treat the rotor fluxes as state variables because they evolve more slowly than stator currents.

$$x = \left[i_{ds}\ i_{qs}\ \lambda_{dr}\ \lambda_{qr}\right]^T \tag{27}$$

$$u = \left[v_{ds}\ v_{qs}\right]^T \tag{28}$$

Using a forward Euler hold over the sampling period T_s

$$\dot{y} = \frac{y(k+1)-y(k)}{T_s} \tag{29}$$

By substituting *eq. (9)* in *(8)*, the discrete-time state update is given as

$$x(k+1) = A_d x(k) + B_d u(k+1) \tag{30}$$

with constant coefficient matrices

$$A_d = I + A_c T_S \tag{31}$$

$$B_d = B_c T_s \tag{32}$$

where the continuous-time matrices are given as

$$A_c = \begin{bmatrix} -\frac{R_s}{\sigma L_s} & \omega_e & \frac{R_s L_m}{\sigma L_s L_r} & 0 \\ -\omega_e & -\frac{R_s}{\sigma L_s} & 0 & \frac{R_s L_m}{\sigma L_s L_r} \\ \frac{L_m R_r}{L_r} & 0 & -\frac{R_r}{L_r} & \omega_{sl} \\ 0 & \frac{L_m R_r}{L_r} & -\omega_{sl} & -\frac{R_r}{L_r} \end{bmatrix} \tag{33}$$

$$B_c = \frac{1}{\sigma L_s}\begin{bmatrix} 1 & 0 \\ 0 & 1 \\ 0 & 0 \\ 0 & 0 \end{bmatrix} \tag{34}$$

Then the stator currents are predicted as

$$i_{ds}(k+1) = \left(1 - \frac{R_s T_s}{\sigma L_s}\right) i_{ds}(k) + T_s \omega_e i_{qs}(k) + \frac{T_s}{\sigma L_s} v_{ds}(k+1) - \frac{L_m T_s}{\sigma L_s L_r} R_r i_{dr}(k) \tag{35}$$

$$i_{qs}(k+1) = \left(1 - \frac{R_s T_s}{\sigma L_s}\right) i_{qs}(k) - T_s \omega_e i_{ds}(k) + \frac{T_s}{\sigma L_s} v_{qs}(k+1) - \frac{L_m T_s}{\sigma L_s L_r} R_r i_{qr}(k) \tag{36}$$

In a practical implementation, it is essential to incorporate a delay compensation mechanism to address errors caused by signal transmission delays and the timing of switching signal application to power electronic devices in simulations, the next switching state is calculated, and the corresponding voltage vector is applied almost instantaneously. However, in real-time systems, there is a finite computation delay before the next control action can be applied, resulting in a one-sampling-period delay in the MPC loop. To accurately estimate the actual current in the $k+2$ control cycle, it becomes necessary to first predict the current for the $k+1$ cycle based on the voltage vector applied during the k cycle. This predicted current is then used as the current value for the $k+1$ cycle during the next computation. Consequently, *equation (7)* must be adapted with a delay compensation strategy to reflect the dynamics of the actual system and ensure accurate current prediction in the presence of control and actuation delays.

Two-step current prediction is given as

$$i_{ds}(k+2) = \left(1 - \frac{R_s T_s}{\sigma L_s}\right) i_{ds}(k+1) + T_s \omega_e i_{qs}(k+1) + \frac{T_s}{\sigma L_s} v_{ds}(k+2) - \frac{L_m T_s}{\sigma L_s L_r} R_r i_{dr}(k+1) \tag{37}$$

$$i_{qs}(k+2) = \left(1 - \frac{R_s T_s}{\sigma L_s}\right) i_{qs}(k+1) - T_s \omega_e i_{ds}(k+1) + \frac{T_s}{\sigma L_s} v_{qs}(k+2) - \frac{L_m T_s}{\sigma L_s L_r} R_r i_{qr}(k+1) \tag{38}$$

Let $\omega_{sl}(k+1) = \omega_e(k+1) - \omega_r(k+1)$

Then rotor flux is predicted as

$$\lambda_{dr}(k+2) = \lambda_{dr}(k+1) + T_s\left(-\frac{R_r}{L_r}\lambda_{dr}(k+1) + \omega_{sl}(k+1)\lambda_{qr}(k+1) + \frac{L_m R_r}{L_r} i_{ds}(k+1)\right) \tag{39}$$

$$\lambda_{qr}(k+2) = \lambda_{qr}(k+1) + T_s\left(-\frac{R_r}{L_r}\lambda_{qr}(k+1) - \omega_{sl}(k+1)\lambda_{dr}(k+1) + \frac{L_m R_r}{L_r} i_{qs}(k+1)\right) \tag{40}$$

Stator flux magnitude at $k+2$ is given as

$$\lambda_{ds}(k+2) = L_s i_{ds}(k+2) + L_m i_{dr}(k+2) \tag{41}$$

$$\lambda_{qs}(k+2) = L_s i_{qs}(k+2) + L_m i_{qr}(k+2) \tag{42}$$

Electromagnetic torque at $k+2$ is given as

$$T_e(k+2) = \frac{3}{2}\frac{P}{2}\left[\lambda_{dr}(k+2) i_{qs}(k+2) - \lambda_{qr}(k+2) i_{ds}(k+2)\right] \tag{43}$$

FOREX Publication
Open Access | Rapid and quality publishing
International Journal of Electrical and Electronics Research (IJEER)
Research Article | Volume 13, Issue 4 | Pages 756-771 | e-ISSN: 2347-470X

In finite-set current-model predictive control (CMPC) of an open-end-winding induction motor (OEW-IM), the two three-phase inverters are treated as a single "virtual" converter whose output is the difference between their pole voltages. With equal and independent DC-link voltages V_{dc} , this virtual converter can generate 19 distinct space-vector positions (18 active plus the zero vector) in the stationary $d-q$ reference frame, as illustrated in *figure 5*. Each point in that hexagon corresponds to one unique combination of the six switch states $(S_{a1}, S_{b1}, S_{c1}, S_{a2}, S_{b2}, S_{c2})$.

During every sampling step the controller assembles the set

$$v = \{v_{dq}^m\}_{m=1}^{19} \tag{44}$$

$$v_{dq}^m = \begin{bmatrix} v_d^m \\ v_q^m \end{bmatrix} \tag{45}$$

and inserts each candidate v_{dq}^m into the two-step prediction model to obtain the corresponding predicted stator-flux magnitude $\lambda_s^m(k+2)$ and predicted electromagnetic torque $T_e^m(k+2)$.

The quality of every candidate is quantified by a quadratic cost function

$$C^m = F_\lambda|\lambda_s^* - \lambda_s^m(k+2)| + F_T|T_e^* - T_e^m(k+2)| \tag{46}$$

Where

- λ_s^* – reference stator-flux magnitude (or indirectly, desired stator-current magnitude),
- T_e^* – reference electromagnetic torque,
- F_λ, F_T – non-negative weighting factors that balance flux-tracking versus torque-tracking priorities and normalize the two error terms.

The voltage vector $v_{dq}^{m_{min}}$ that minimizes *eq. (11)*

$$m_{min} = argmin\ C^m \tag{47}$$

is selected as the reference voltage for the virtual OEW converter, and the corresponding pair of inverter switch states is queued. After the inherent computation-and-PWM delay, those switches are applied in the next control period, ensuring that the machine receives precisely the voltage for which currents, fluxes and torque were predicted two steps earlier.

This procedure simultaneously exploits the enlarged voltage set of the OEW topology and compensates one-step hardware delay, enabling fast, high-accuracy torque and flux control of the induction motor.

5. PROPOSED MPC–SVM SCHEME

To embed space-vector modulation (SVM) inside the finite-set MPC loop of an open-end-winding induction motor (OEW-IM), the controller must first estimate the angle of the stator-voltage vector that will be required one sampling period ahead. Starting from the discrete-time stator-voltage model and using the already-predicted currents at instant $k+1$, the components of the voltage vector to be applied at $k+2$ are

$$\hat{v}_{ds} = \left(R_s + \frac{\sigma L_s}{T_s}\right) i_{ds}(k+1) - \sigma L_s \omega_e i_{qs}(k+1) + \frac{L_m}{T_s}[i_{dr}(k+1) - i_{dr}(k)] \tag{48}$$

$$\hat{v}_{qs} = \left(R_s + \frac{\sigma L_s}{T_s}\right) i_{qs}(k+1) - \sigma L_s \omega_e i_{ds}(k+1) + \frac{L_m}{T_s}[i_{qr}(k+1) - i_{qr}(k)] \tag{49}$$

Then the voltage angle can be predicted as

$$\theta_v = \tan^{-1}\left(\frac{\hat{v}_{qs}}{\hat{v}_{ds}}\right) \tag{50}$$

In the proposed MPC–SVM strategy for driving the Open-End Winding Induction Motor (OEWIM), a significant reduction in computational burden is achieved by restricting the number of voltage vectors evaluated during each control cycle. Traditional finite-set MPC methods that rely on evaluating a large set of pre-defined candidate switching vectors often impose a high computational load on microcontrollers, especially when operating at high sampling rates. To address this issue, the proposed method utilizes virtual voltage vector generation, guided by the predicted voltage angle, thereby eliminating the need to evaluate all possible vectors across the full 360° space.

Instead of using all possible switching combinations, the algorithm first estimates the required voltage angle (θ_v) based on the predicted stator current in the next control interval. Around this voltage angle, only three angular sectors are considered: the central angle (θ_v) and two neighboring angles ($\theta_v \pm \theta_d$), where θ_d is a user-defined angular deviation. Within each of these three sectors, N equally spaced virtual voltage vectors are generated, significantly narrowing the search space. Without applying this deadbeat restriction, the number of vectors that would be generated over the full circle is computed as:

$$G(N) = \frac{360^o}{\theta_d}(N-1) + 1 \tag{51}$$

where the additional 1 account for the inclusion of the zero vector. However, by limiting the search to just the three angular sectors, the number of vectors becomes:

$$G_{DB}(N) = 3(N-1) + 1 \tag{52}$$

For example, with $\theta_d = 15^o$ and $N = 7$, the required number of vector evaluations drops from 337 to just 19, reducing the computational effort even below that of a conventional MPC.

Each virtual vector is mathematically constructed using its position index $x \in \{1, 2, \ldots, N\}$ and is scaled based on the sum of the two inverter DC-link voltages V_{dc1} and V_{dc2}. The virtual voltage components in the stationary reference frame are calculated using:

$$v_{ds}^{vir} = \frac{V_{dc1}+V_{dc2}}{\sqrt{3}} \cdot x \cdot \cos(\theta_v \pm \theta_d) \tag{53}$$

FOREX Publication
Open Access | Rapid and quality publishing
International Journal of Electrical and Electronics Research (IJEER)
Research Article | Volume 13, Issue 4 | Pages 756-771 | e-ISSN: 2347-470X

$$v_{qs}^{vir} = \frac{V_{dc1}+V_{dc2}}{\sqrt{3}} \cdot x \cdot \sin(\theta_v \pm \theta_d) \quad (54)$$

where only one instance of the zero vector ($x = 0$) is included to prevent redundancy. These virtual vectors are treated as candidates for input voltages in the MPC cost function, replacing the need to simulate all physical switching states.

The proposed MPC–SVM approach retains the same current prediction model and cost function formulation as the conventional finite-set MPC developed for the OEWIM. However, by focusing only on a small, intelligently chosen subset of virtual voltage vectors, the method achieves a near-optimal control action with much lower computational complexity. This makes the method highly suitable for real-time embedded control systems with limited processing power while ensuring fast dynamic response and accurate torque and flux tracking in OEWIM drives.

In the dual-inverter open-end-winding induction-motor (OEWIM) configuration, each three-phase bridge is a voltage-source inverter (VSI). To avoid shoot-through during commutation, every VSI inserts a dead time between the turn-off of one device and the turn-on of its complementary switch. Although indispensable for reliability, this delay distorts the commanded phase voltages, introducing a nonlinear error that degrades current quality and, ultimately, torque accuracy. Even with modern fast-switching devices, compensating for dead-time effects remains essential in high-performance torque-controlled drives.

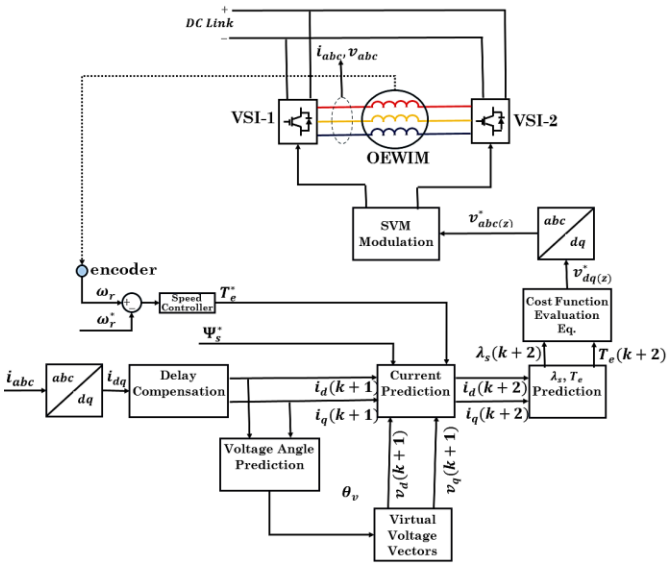

Figure 6. Control strategy of the MPC-SVM for OEWIM

In the proposed MPC–SVM scheme the optimal reference voltage obtained from the prediction stage is synthesized with space-vector modulation (SVM): two adjacent active vectors and the zero vector are time-weighted within the sampling period to reproduce the desired magnitude and phase. Compared with the finite-set CMPC approach, the continuous freedom of SVM yields a smoother voltage waveform, lower current ripple and hence steadier electromagnetic torque.

A simple feed-forward dead-time compensation corrects the reference before it is fed to the PWM modulators:

$$v_{dead(z)} = \frac{T_{dead}}{T_s} v_{dc}(z) \quad (55)$$

$$v^*_{abc1_d} = v_{abc1} + \beta_{abc} v_{dead(1)} \quad (56)$$

$$v^*_{abc2_d} = v_{abc2} + \beta_{abc} v_{dead(2)} \quad (57)$$

$$\beta_{abc} = \begin{cases} +1, & i_{abc} > 0 \\ -1, & iabc < 0 \end{cases} \quad (58)$$

Figure 6 summarizes the complete control structure: the discrete-time current predictor supplies the MPC cost-minimization block, whose optimal voltage vector is angle-tracked by the SVM routine; reference-splitting and dead-time compensation follow, after which the corrected three-phase voltages are compared with high-frequency carriers to generate the dual-inverter gating signals. Together, these stages ensure that delay-compensated model prediction, smooth SVM synthesis, and precise dead-time correction cooperate to deliver high-fidelity torque control of the OEW induction motor.

6. SIMULATION RESULTS

To assess the performance and effectiveness of the proposed Beluga Whale Optimization (BWO) algorithm-based Maximum Power Point Tracking (MPPT) strategy for a photovoltaic (PV) system feeding an Open-End Winding Induction Motor (OEWIM) drive with improved Model Predictive Control–Space Vector Modulation (MPC-SVM), a comprehensive simulation study was conducted. The system configuration used for the simulation is illustrated in *figure 1*, encompassing all the essential components of the proposed control architecture. This setup facilitates a holistic evaluation of the system's behavior under various dynamic and steady-state operating conditions.

The control strategy implemented for the improved MPC-SVM of the OEWIM is detailed in *figure 6*. This advanced predictive modulation framework is critical in enhancing the dynamic response and significantly minimizing torque ripple across the full range of motor operation. By effectively determining the optimal voltage vectors using space vector modulation principles and predictive current control, the drive achieves smoother torque output and improved transient performance.

The proposed BWO algorithm is seamlessly integrated into the PV-side MPPT module. Its operational steps are delineated in the pseudo-code presented in *sub-section 3.1.4* , which outlines the iterative search mechanism employed to locate the global maximum power point (MPP) of the PV system under varying irradiance and temperature conditions. The BWO's efficient exploration-exploitation balance ensures rapid convergence to the MPP with minimal oscillation, enhancing the stability and responsiveness of the power conversion chain.

Through the use of this BWO-based MPPT algorithm, the PV system is continuously operated at its optimal power generation point. This ensures that the OEWIM drive receives the

FOREX Publication
Open Access | Rapid and quality publishing
International Journal of Electrical and Electronics Research (IJEER)
Research Article | Volume 13, Issue 4 | Pages 756-771 | e-ISSN: 2347-470X

maximum available electrical energy, thereby improving overall drive efficiency. Moreover, the combination of BWO and MPC-SVM creates a synergistic effect—optimizing both power extraction and motor performance simultaneously.

The electrical and mechanical parameters of the OEWIM used in the simulation are summarized in *table 1*. These parameters are selected to reflect typical industrial motor characteristics, providing a realistic basis for evaluating the control scheme's applicability in practical deployments.

The simulation outcomes demonstrate the effectiveness of the proposed strategy in achieving superior performance across several metrics including torque ripple reduction, dynamic response improvement, and maximum power tracking efficiency. Overall, the integration of the BWO-based MPPT with an improved MPC-SVM control for the OEWIM drive results in a robust, efficient, and adaptable system suitable for modern solar-powered electric drive applications.

Table 1. Simulation Parameters

OEWIM	
Nominal power, voltage (line-line), and frequency	6 HP, 230 V, 50 Hz
Stator resistance and inductance	0.466 Ω, 3.03 mH
Rotor resistance and inductance	0.2873 Ω, 2.02 mH
Mutual inductance	47 mH
Inertia, friction factor, pole pairs	0.0279, 6.41×10^{-4}, 2
PV Array	
Module	E&H EHS3-238
Maximum Power	238.091 W
Cells per module	60
Open circuit voltage	37.3 V
Short-circuit current	8.53 A
Voltage at maximum power point	30.1 V
Current at maximum power point	7.91 A
Temperature coefficient of open circuit voltage	-0.3481 %/deg.C
Temperature coefficient of short circuit current	0.042204 %/deg.C
Parallel strings	2
Series-connected modules per string	10
BWO Optimization	
Maximum Iterations	100
Population Size	50
Problem Dimension (dim)	1
Lower and Upper Bound (lb, ub)	0, 1

***Case 1*: Performance Analysis Under Constant Irradiance and Reference Speed**

This case investigates steady-state behaviour when the PV array is illuminated at 1000 W/m^2 and the OEWIM is commanded to maintain 1500 RPM while delivering a 5 Nm mechanical load. The aim is to benchmark the BWO MPPT against three widely cited algorithms—Perturb-and-Observe (P&O), Particle Swarm Optimization (PSO) and Cuckoo Optimization Algorithm (COA).

Figure 7 plots the PV terminal voltage. With BWO, the voltage settles rapidly to its reference with negligible ripple, whereas P&O, PSO and COA suffer pronounced overshoot, larger oscillatory envelopes and longer settling times, all of which penalize conversion efficiency. The corresponding DC-link profiles in *figure 8* confirm this tendency. The BWO-controlled link exhibits a short rise time and minimal steady-state ripple; the conventional methods display sluggish voltage build-up and persistent ripple, signaling poorer energy transfer and greater stress on capacitive components.

Figures 9 and *10* compare the PV power output and the power delivered to the voltage-source converter (VSC). Due to accurate global-peak tracking, the BWO strategy extracts a consistently higher wattage and transfers it to the VSC with lower loss, whereas the reference algorithms lose power because they drift away from the true MPP even under constant irradiance.

Figure 11 shows the motor-speed trajectory. Under BWO the OEWIM reaches 1500 RPM sooner, with a shorter settling period and almost imperceptible speed ripple. PSO, COA and P&O exhibit delayed acceleration, extended settling and noticeable speed wavering. The corresponding electromagnetic-torque waveforms in *figure 12* reveal that BWO also suppresses torque ripple more effectively throughout the transient.

Table 2 consolidates these findings by listing the rise time t_r , peak overshoot M_p, settling time t_s, steady-state ripple R_{ss}, steady-state error e_{ss} and overall efficiency η for the DC-link voltage, motor speed and torque. Across every metric the proposed BWO algorithm delivers superior or comparable performance—shorter t_r and t_s, lower M_p, reduced R_{ss} and e_{ss}, and the highest conversion efficiency—demonstrating its robustness and suitability for PV-fed OEWIM drives operating under fixed environmental conditions. To statistically validate the performance of the BWO algorithm, 30 independent simulation runs under varying initial conditions or conducted. The results are now presented in the *table 3*. This table provides the mean and standard deviation for all key performance indices, including the Mean Absolute Error (MAE).

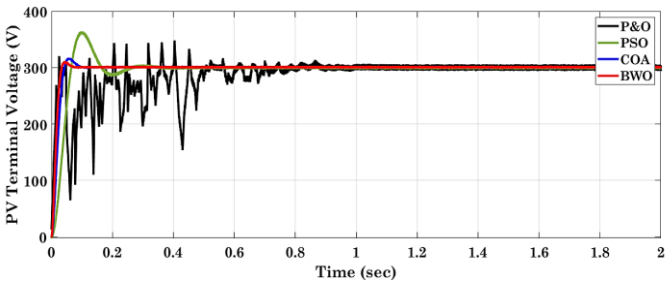

Figure 7. PV terminal voltage at 1000 w/m^2 irradiance

FOREX Publication
Open Access | Rapid and quality publishing
International Journal of Electrical and Electronics Research (IJEER)
Research Article | Volume 13, Issue 4 | Pages 756-771 | e-ISSN: 2347-470X

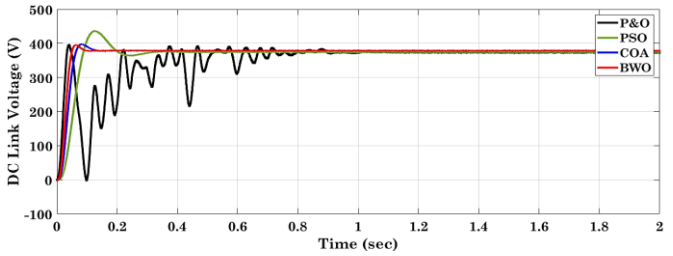

Figure 8. DC link voltage

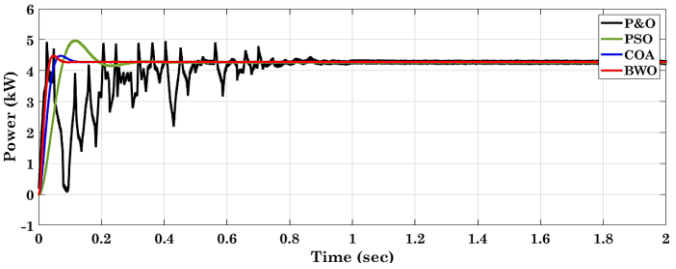

Figure 9. PV generated power at 1000 w/m^2 irradiance

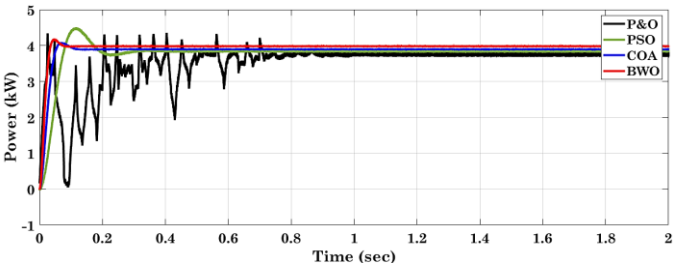

Figure 10. Power transferred to VSC's from PV system

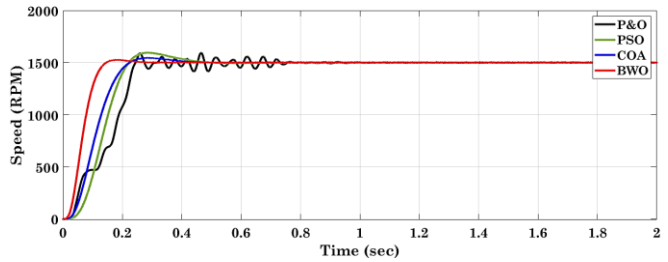

Figure 11. Speed of OEWIM with conventional and proposed algorithm at 1500RPM reference speed and 1000 w/m^2 irradiance

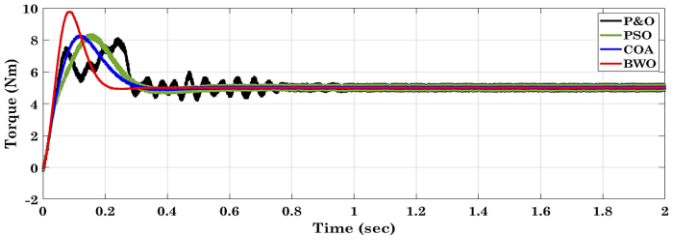

Figure 12. Torque of OEWIM with conventional and proposed algorithm at 1500RPM reference speed and 1000 w/m^2 irradiance

Table 2. Transient behaviour of DC link voltage, speed, and torque ripples with proposed and conventional algorithms in terms of Rise Time (t_r) in seconds, peak Overshoot (M_p) in %, Settling Time (t_s) in seconds, Steady State Ripples (R_{ss}) in %, Steady State Error (e_{ss}) in % and efficiency (η) in %.

		P&O	PSO	COA	BWO
DC Link Voltage	t_r	0.29	0.238	0.216	0.148
	M_p	7.36	6.52	2.96	2.05
	t_s	1.35	0.91	0.68	0.31
	R_{ss}	5.11	4.13	2.68	1.45
	e_{ss}	1.15	0.74	0.58	0.26
Speed	t_r	0.26	0.25	0.225	0.154
	M_p	7.02	6.95	3.4	2.15
	t_s	1.1	0.85	0.7	0.48
	R_{ss}	4.85	4.32	3.56	1.25
	e_{ss}	1.02	0.86	0.42	0.23
Torque	R_{ss}	5.6	4.2	2.2	1.5
Efficiency	η	97.25	98.36	98.75	99.02

Table 3. Statistical performance comparison of algorithms over 30 simulation runs. (Mean ± Standard Deviation)

		P&O	PSO	COA	BWO	% improvement of BWO over COA
DC Link Voltage	t_r	0.295± 0.021	0.242± 0.018	0.221± 0.015	0.151± 0.008	31.7 %
	t_s	1.38±0. 11	0.94±0. 09	0.71±0. 07	0.32±0. 04	54.9 %
	R_{ss}	5.15±0. 32	4.18±0. 28	2.72±0. 21	1.48±0. 12	45.6 %
	MAE	1.42±0. 15	0.89±0. 11	0.71±0. 09	0.29±0. 05	59.2 %
Speed	R_{ss}	4.91±0. 35	4.38±0. 31	3.61±0. 25	1.28±0. 10	64.5 %
	e_{ss}	1.05±0. 08	0.88±0. 07	0.45±0. 06	0.24±0. 03	46.7 %
	MAE	1.28±0. 13	0.95±0. 10	0.62±0. 08	0.31±0. 04	50.0 %
Torque	R_{ss}	5.65±0. 40	4.25±0. 33	2.25±0. 20	1.52±0. 15	32.4 %
Efficiency	η	97.20± 0.25	98.31± 0.22	98.72± 0.18	98.98± 0.15	0.26 %

Case 2: Performance Analysis Under Variable Irradiance and Constant Reference Speed

In the second study the Open-End Winding Induction Motor (OEWIM) drive is evaluated while the solar input follows a deliberately aggressive irradiance profile (*figure 13*) and the mechanical reference speed is held at 1470 RPM with a constant 5 N m load. Irradiance starts at 300 W/m^2, steps to 500 W/m^2 at 1.5 s, 700 W/m^2 at 3.5 s, 900 W/m^2 at 5.5 s, and finally peaks at 1000 W/m^2 before settling to 800 W/m^2 after 8 s. This sequence imposes rapid, wide-range power fluctuations that test both the BWO MPPT and the delay-compensated MPC–SVM current controller.

FOREX Publication
Open Access | Rapid and quality publishing
International Journal of Electrical and Electronics Research (IJEER)
Research Article | Volume 13, Issue 4 | Pages 756-771 | e-ISSN: 2347-470X

Figures 14 and *15* show the PV terminal voltage and the DC-link voltage, respectively. Despite the steep irradiance transitions, the BWO MPPT keeps the PV operating point on the instantaneous maximum-power locus, so both voltages remain tightly regulated with scant overshoot and negligible ripple. In earlier simulations with Perturb-and-Observe, Particle Swarm and Cuckoo-based trackers, each step-in irradiance produced pronounced voltage sag-and-recover cycles; those artefacts are virtually absent under BWO, demonstrating its superior tracking agility.

The corresponding power waveforms in *figure 16* underlines this advantage. PV output power rises and falls in proportion to solar input, yet the BWO algorithm extracts the available energy with high fidelity, while the battery seamlessly covers any shortfall. *Figure 17* details this dual-mode behaviour: between 1.5 s and 6.5 s the battery discharges to support the motor, then switches to charging when irradiance exceeds the mechanical demand, efficiently banking surplus energy for later use.

Mechanical responses are plotted in *figures 18* and *19*. The motor speed tracks its 1470 RPM reference with sub-1 % deviation throughout the entire irradiance sweep, and torque shows only minor oscillations, attesting to the robustness of the MPC–SVM scheme. Stator current waveforms (*figure 20*) remain sinusoidal and well balanced, indicating that the predictive controller and space-vector modulator continue to supply clean three-phase excitation even as the available DC power fluctuates.

Collectively, the results confirm that the proposed BWO-driven MPPT, together with the improved MPC-SVM control of the OEWIM, forms a resilient and efficient energy-conversion chain. The architecture successfully reconciles abrupt solar-power variability with stringent motor-drive requirements, maintaining voltage stability, suppressing torque ripple, and ensuring precise speed regulation—all while optimally managing battery charge and discharge events.

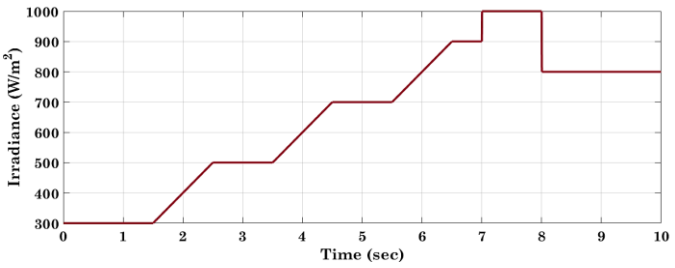

Figure 13. Variation of irradiance

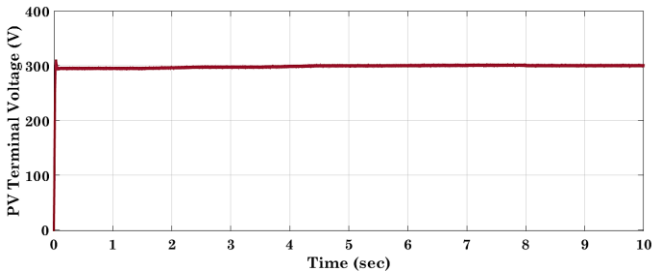

Figure 14. PV terminal voltage for irradiance variation

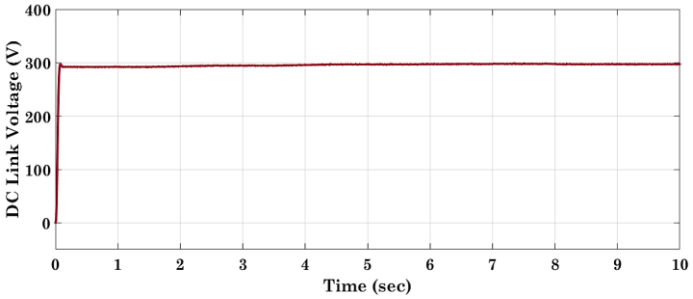

Figure 15. DC link voltage for irradiance variation

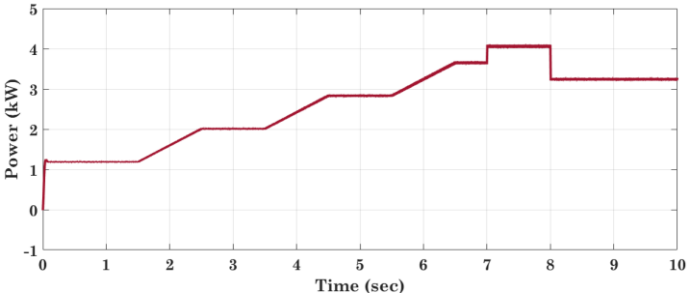

Figure 16. Power transferred to VSC's from PV system for irradiance variation

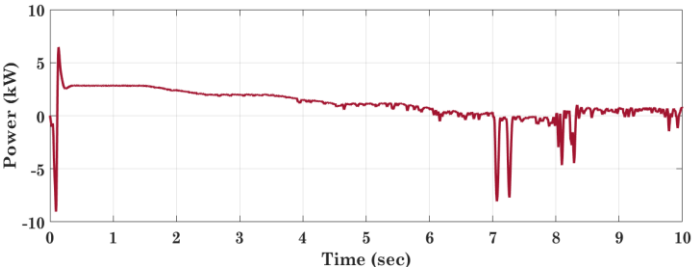

Figure 17. Battery power transfer

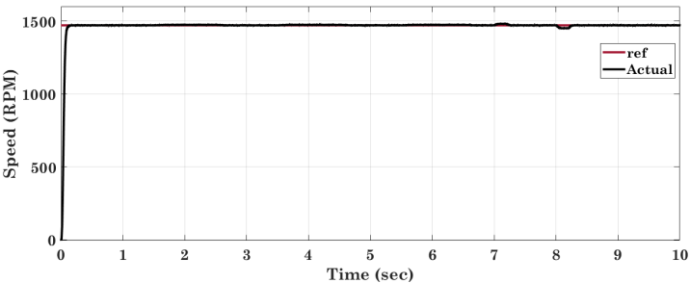

Figure 18. Speed of OEWIM with proposed algorithm at 1470RPM reference speed and irradiance variation

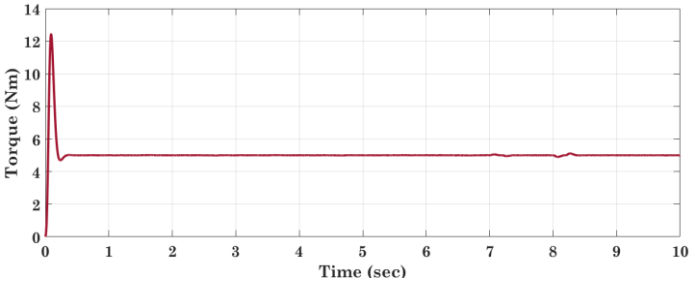

Figure 19. Torque of OEWIM with proposed algorithm at 1500RPM reference speed and irradiance variation

FOREX Publication
Open Access | Rapid and quality publishing
International Journal of Electrical and Electronics Research (IJEER)
Research Article | Volume 13, Issue 4 | Pages 756-771 | e-ISSN: 2347-470X

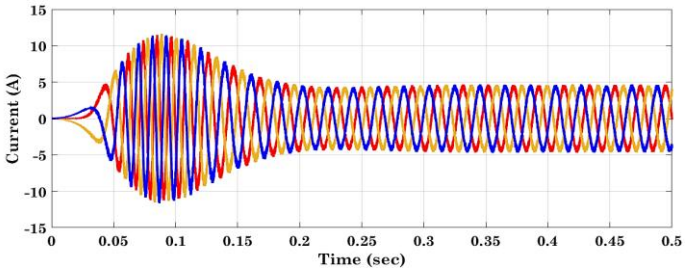

Figure 20. Stator winding current of OEWIM with proposed algorithm at 1500RPM reference speed and irradiance variation

Case 3: Performance Analysis Under Constant Irradiance and Variable Reference Speed

In the final scenario the photovoltaic array is held at 1000 W/m^2 while the OEWIM is driven through an aggressive speed schedule that mirrors real-world load fluctuations. The reference speed begins at 1500 RPM (0–1.5s), steps down successively to 1200, 900 and 700 RPM, plunges to 500 RPM at 4.5s, drifts to 400 RPM and holds until 7.5s, rises to 600 RPM (7.5–9s) and finally jumps to 1200 RPM. As presented in figure 20, throughout these abrupt transitions the proposed MPC–SVM drive, supplied by the Beluga-Whale-optimized MPPT, maintains excellent tracking: steady-state speed ripple is limited to 0.95 %, peak overshoot to 0.83 %, the fastest step exhibits a 140ms rise time, and all steps settle within 280ms.

Torque waveforms (*figure 21*) remain smooth thanks to the five-level hysteresis band embedded in the direct-torque layer of the controller, while stator currents recorded between 1s and 3s (*figure 22*) stay balanced and nearly sinusoidal, evidencing sound flux orientation even during rapid deceleration.

Because irradiance is constant the PV array delivers a stable electrical output (*figure 23*). Motor power demand, however, swings with the speed commands *(figure 24*). Whenever demand exceeds PV supply, the battery shifts seamlessly into discharge mode; when demand falls, the surplus energy is diverted to recharge the battery. This bidirectional power exchange showcases the tight coordination among the BWO MPPT, predictive motor control, and energy-storage management, yielding optimal utilization of solar energy while ensuring uninterrupted drive operation.

Overall, Case 3 demonstrates that the proposed hybrid architecture combines precise speed regulation, low torque ripple, and efficient energy balancing, confirming its suitability for renewable-powered drives subject to highly variable load conditions.

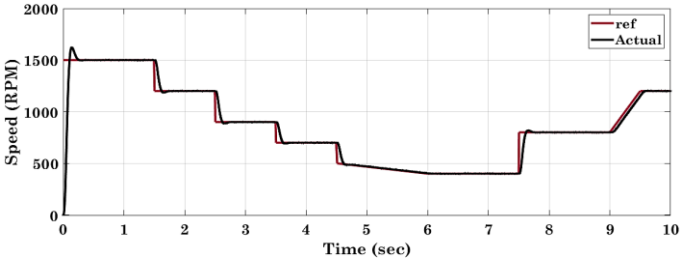

Figure 20. Speed of OEWIM with proposed algorithm with variable reference speed and constant irradiance

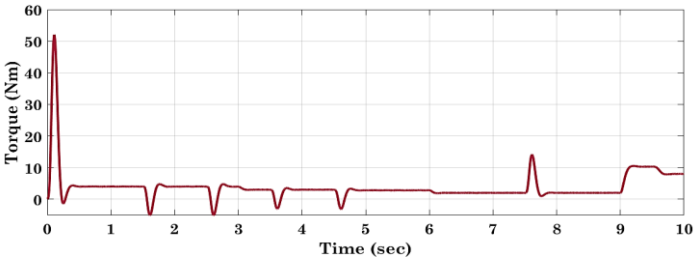

Figure 21. Torque of OEWIM with proposed algorithm with variable reference speed and constant irradiance

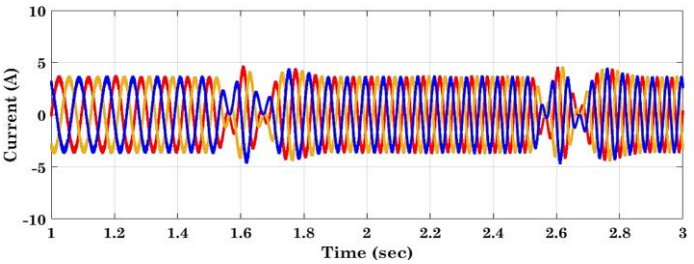

Figure 22. Stator winding current of OEWIM with proposed algorithm between 3 to 4 seconds

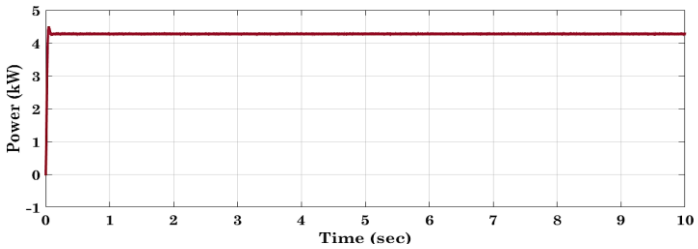

Figure 23. Power transferred to VSC's from PV system with variable reference speed and constant irradiance

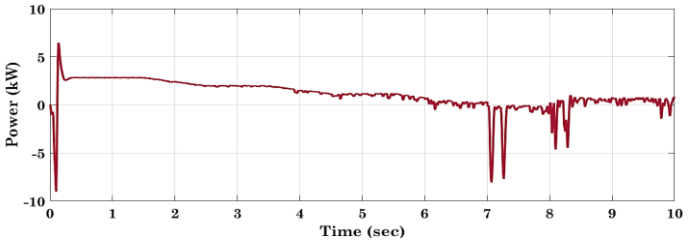

Figure 24. Battery terminal power with proposed algorithm with variable reference speed and constant irradiance

A primary limitation of this study is its validation through simulation software without experimental or Hardware-in-the-Loop (HIL) testing. This approach was selected to enable a controlled, comprehensive, and cost-effective proof-of-concept for the complex multi-algorithmic system. While the simulation environment provides valuable insights, it inherently idealizes certain aspects, such as sensor noise, component tolerances, and communication delays in a real-time controller. The computational load of the combined BWO and MPC-SVM algorithms, while designed for efficiency, has not been benchmarked on a physical digital signal processor (DSP).

Despite these limitations, the practical feasibility of the proposed framework is strongly supported by its structure, which is composed of deterministic mathematical operations well-suited

FOREX Publication
Open Access | Rapid and quality publishing
International Journal of Electrical and Electronics Research (IJEER)
Research Article | Volume 13, Issue 4 | Pages 756-771 | e-ISSN: 2347-470X

for implementation on modern DSPs or FPGAs. The results thus provide a high-confidence foundation for the system's viability. Therefore, the immediate and critical future work is the real-time HIL implementation of this co-designed framework to experimentally validate its performance and computational requirements. Subsequent research will explore the incorporation of online parameter estimation to enhance robustness and extend the approach with machine learning for proactive fault prediction and system health management.

7. CONCLUSION

This paper presents an efficient control framework for photovoltaic (PV)-fed Open-End Winding Induction Motor (OEWIM) drives using a novel Beluga Whale Optimization (BWO)-based Maximum Power Point Tracking (MPPT) technique, integrated with an improved Model Predictive Control – Space Vector Modulation (MPC–SVM) strategy. The proposed system addresses key challenges in renewable-powered motor drives, such as maximizing solar energy extraction, ensuring dynamic speed tracking, and maintaining power stability under varying operating conditions. Through extensive simulations conducted in MATLAB/Simulink, the performance of the BWO-based MPPT under diverse operating scenarios was rigorously validated and compared with conventional MPPT algorithms like Perturb and Observe (P&O), Particle Swarm Optimization (PSO), and Cuckoo Optimization Algorithm (COA). Across all test cases, including constant irradiance with fixed speed, variable irradiance with constant speed, and constant irradiance with dynamic speed profiles, the proposed method consistently outperformed conventional approaches in terms of Enhanced MPPT accuracy, Superior voltage and power stability, Improved dynamic motor response, Reduced torque ripples and smooth stator current waveforms, and Effective power balancing. Battery with a bidirectional converter that seamlessly transitions between charging and discharging, ensuring continuous operation even during PV power fluctuations. The BWO algorithm proved highly effective at identifying the global optimum operating point of the PV system, resulting in more consistent energy transfer to the OEWIM drive. Meanwhile, the predictive control mechanism ensured fast and precise response to speed variations, making the system highly adaptable for real-time industrial applications. The integration of BWO-based MPPT with MPC–SVM motor control and energy storage creates a robust and intelligent drive system, capable of handling both environmental and load-induced disturbances. The proposed architecture is especially well-suited for applications such as solar-powered electric drives, sustainable transportation systems, and smart industrial automation where efficiency, adaptability, and reliability are critical. Future work may extend this approach to incorporate machine learning-based fault prediction and real-time hardware-in-the-loop implementation for experimental validation.

REFERENCES

[1] Nezamisavojbolaghi, M., Davodian, E., Bouich, A., & Tlemçani, M. (2023). Characterization and Sensitivity Analysis of a Photovoltaic Panel. *Advanced Energy Conversion Materials*, 164-173.

[2] Avesh, M., Hossain, I., & Sharma, R. C. (2024). Revolutionizing transportation: The future impact of green energy. In *Dynamics of transportation ecosystem, modeling, and control* (pp. 261-293). Singapore: Springer Nature Singapore.

[3] Arrozy, J. (2023). Exploring Multiphase Inverters for Open-Winding Machine Drives: Topologies, Fault Tolerance, and Impacts of Modulation Techniques.

[4] Chakrabarti, A., Saha, A., & Biswas, S. K. (2021). Winding open-circuit fault-tolerant operation of single DC-link dual-inverter fed three-phase open-end induction motor drive. *IET Power Electronics*, *14*(7), 1256-1270.

[5] Valencia, D. F., Tarvirdilu-Asl, R., Garcia, C., Rodriguez, J., & Emadi, A. (2021). Vision, challenges, and future trends of model predictive control in switched reluctance motor drives. *IEEE Access*, *9*, 69926-69937.

[6] Hoggui, A., Benachour, A., Madaoui, M. C., & Mahmoudi, M. O. (2024). Comparative Analysis of Direct Torque Control with Space Vector Modulation (DTC-SVM) and Finite Control Set-Model Predictive Control (FCS-MPC) of Five-Phase Induction Motors. *Progress in Electromagnetics Research B*, *108*

[7] Chang, C. C. W., Ding, T. J., Bhuiyan, M. A. S., Chao, K. C., Ariannejad, M., & Yian, H. C. (2023). Nature-inspired optimization algorithms in solving partial shading problems: a systematic review. *Archives of computational methods in engineering*, *30*(1), 223-249.

[8] Zhong, C., Li, G., & Meng, Z. (2022). Beluga whale optimization: A novel nature-inspired metaheuristic algorithm. *Knowledge-based systems*, *251*, 109215.

[9] Mhanni, Y., & Lagmich, Y. (2024). Adaptive metaheuristic strategies for optimal power point tracking in photovoltaic systems under fluctuating shading conditions. *EPJ Photovoltaics*, *15*, 31.

[10] Huang, K. H., Chao, K. H., Kuo, Y. P., & Chen, H. H. (2023). Maximum power point tracking of photovoltaic module arrays based on a modified gray wolf optimization algorithm. *Energies*, *16*(11), 4329.

[11] Rojas-Galván, R., García-Martínez, J. R., Cruz-Miguel, E. E., Álvarez-Alvarado, J. M., & Rodríguez-Resendiz, J. (2024). Performance Comparison of Bio-Inspired Algorithms for Optimizing an ANN-Based MPPT Forecast for PV Systems. *Biomimetics*, *9*(10), 649.

[12] Liu, T., Liu, S., Yu, H., Wu, Z., Tong, J., & Yuan, Q. (2024). Research on Hybrid Approach for Maximum Power Point Tracking of Photovoltaic Systems under Various Operating Conditions. *Electronics*, *13*(19), 3880.

[13] Worku, M. Y., Hassan, M. A., Maraaba, L. S., Shafiullah, M., Elkadeem, M. R., Hossain, M. I., & Abido, M. A. (2023). A comprehensive review of recent maximum power point tracking techniques for photovoltaic systems under partial shading. *Sustainability*, *15*(14), 11132.

[14] Ali, H. H., Ebeed, M., Fathy, A., Jurado, F., Babu, T. S., & A. Mahmoud, A. (2023). A new hybrid multi-population GTO-BWO approach for parameter estimation of photovoltaic cells and modules. *Sustainability*, *15*(14), 11089.

[15] You, G., Lu, Z., Qiu, Z., & Cheng, H. (2024). AMBWO: An Augmented Multi-Strategy Beluga Whale Optimization for Numerical Optimization Problems. *Biomimetics*, *9*(12), 727.

[16] Du, W., Peng, S. T., Wu, P. S., & Tseng, M. L. (2024). High-accuracy photovoltaic power prediction under varying meteorological conditions: enhanced and improved beluga whale optimization extreme learning machine. *Energies*, *17*(10), 2309.

[17] Mousavi, M. S., Davari, S. A., Flores-Bahamonde, F., Garcia, C., & Rodriguez, J. (2023). Sampling error-based model-free predictive current control of open-end winding induction motor with simplified vector selection. *IET Electric Power Applications*, *17*(3), 358-369.

[18] Cataldo, P., Jara, W., Riedemann, J., Pesce, C., Andrade, I., & Pena, R. (2023). A predictive current control strategy for a medium-voltage open-end winding machine drive. *Electronics*, *12*(5), 1070.

[19] Praveen Kumar, K. V., & Vinay Kumar, T. (2018). Predictive torque control of open-end winding induction motor drive fed with multilevel inversion using two two-level inverters. *IET Electric Power Applications*, *12*(1), 54-62.

[20] Geng, Y., Han, P., Chen, X., Chen, R., Le, Z., & Lai, Z. (2021). On-line dead-time compensation method for dual three phase PMSM based on adaptive notch filter. *IET Power Electronics*, *14*(15), 2452-2465.

International Journal of Electrical and Electronics Research (IJEER)
Research Article | Volume 13, Issue 4 | Pages 756-771 | e-ISSN: 2347-470X

[21] Yuan, D., Zhang, X., Yin, Z., Jia, X., & Gao, Y. (2023, November). A Strategy for Improving Dead-Time Performance of Induction Motor Based on SiC MOSFET. In *International Joint Conference on Energy, Electrical and Power Engineering* (pp. 316-322). Singapore: Springer Nature Singapore.

[22] Son, D. I., Han, J. S., Park, J. S., Lim, H. S., & Lee, G. H. (2023). Performance improvement of dtc-svm of pmsm with compensation for the dead time effect and power switch loss based on extended kalman filter. *Electronics*, *12*(4), 966.

[23] Mohammed, H. M., Umar, S. U., & Rashid, T. A. (2019). A systematic and meta-analysis survey of whale optimization algorithm. *Computational intelligence and neuroscience*, *2019*(1), 8718571.